ELSEVIER

Volume 184, Issue 4, April 2011

JOURNAL OF SOLID STATE CHEMISTRY

www.elsevier.com/locate/jssc

CONTENTS

Abstracted/indexed in BioEngineering Abstracts, Chemical Abstracts, Coal Abstracts, Current Contents/Physics, Chemical, & Earth Sciences, Engineering Index, Research Alert, SCISEARCH, Science Abstracts, and Science Citation Index. Also covered in the abstract and citation database SCOPUS®. Full text available on ScienceDirect®.

Regular Articles

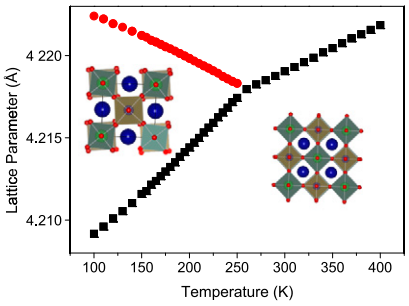

The tetragonal–cubic phase transition observed in the cation ordered double perovskite Ba_2YTaO_6 is inhibited when these are disordered.

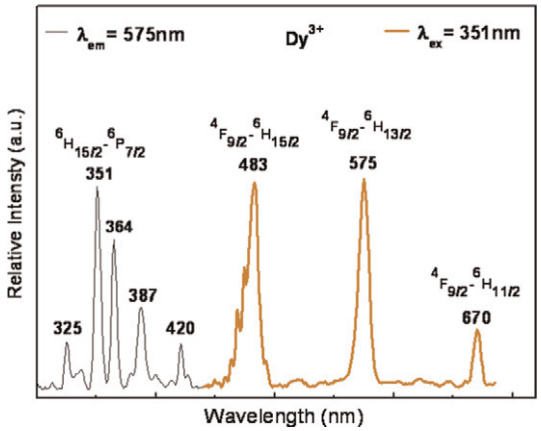

Among the fifteen isostructural $A_2Mo_4Sb_2O_{18}$ (A = rare earth metal) molybdoantimonites, eight (A = Pr, Sm, Eu, Tb, Dy, Ho, Er, Tm) compounds exhibit neat characteristic lanthanide photoluminescence in the 200–800 nm range at room temperature.

Regular Articles—Continued

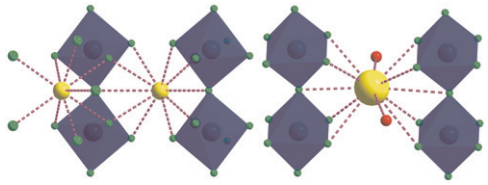

Ball-and-stick and polyhedral representations for (a) β-K_2TiF_5 and (b) $Rb_2TiF_5 \cdot H_2O$ or $Cs_2TiF_5 \cdot H_2O$ with the K^+ and Rb^+ (or Cs^+) coordination environment emphasized.

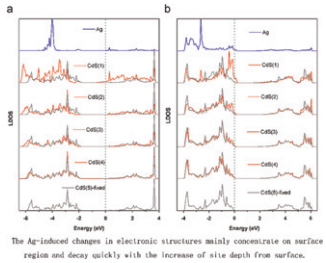

We studied the adsorption of Ag at Cd-terminated CdS (0 0 0 1) and S-terminated CdS (0 0 0 $\bar{1}$) surfaces as a function of Ag coverage by means of the first-principles calculations. In addition, related properties of Ag cluster adsorption at Cd-terminated (0 0 0 1) surface are also discussed. Our *ab initio* calculations are useful complement to the intense experimental studies for Ag@CdS interface.

Continued

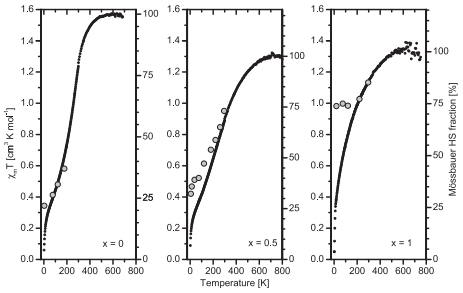

Comparison of fractions of high spin Fe(II) from Mössbauer spectra (circles) with plots of $\chi_m T$ (dots) versus T. Discrepancies between both methods indicate anti-ferromagnetic spin coupling.

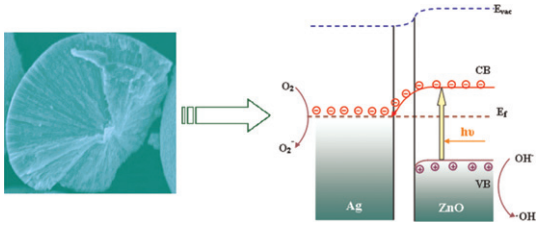

A green strategy is report to construct Ag/ZnO metal–semiconductor nanocomposites with hierarchical micro/nanostructure and enhanced photocatalytic activity.

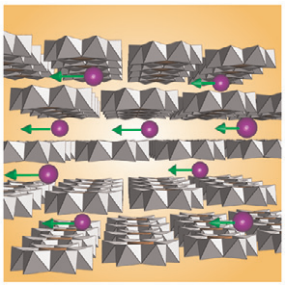

Two compounds $Na_{2.5}K_{5.3}[SbW_6O_{24}](NO_3)_{0.8} \cdot 12H_2O$ (**1**) and $Na_2K_{5.35}[SbW_6O_{24}]Cl_{0.35} \cdot 12H_2O$ (**2**) possessing a layer-like Anderson (LLA) structure exhibited pseudo intercalation-deintercalation behavior. The dehydrated form of **1** is a high alkaline cation conductor with a conductivity of $1.2 \times 10^{-2}\ \Omega^{-1}\ cm^{-1}$ at 400 °C.

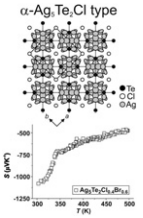

A structure section of the α-Ag_5Te_2Cl structure type and the thermopower evolution of $Ag_5Te_2Cl_{0.4}Br_{0.6}$ undergoing a silver ion order/disorder phase transition.

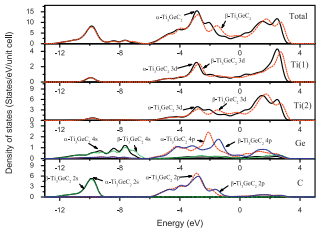

The less phase stability of β- Ti_3 SiC_2 compared to that of α- Ti_3 SiC_2 can be interpreted by the states between −6.0 and 3.6 eV shift toward the higher energy region for β- Ti_3 SiC_2.

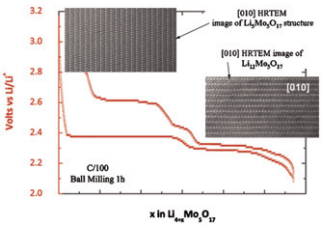

Structure determination of the fully intercalated phase $Li_{12}Mo_5O_{17}$ and of the deintercalated oxide $Li_5Mo_5O_{17}$ has been carried out by electron microscopy and neutron powder diffraction. The reversible topotactic transformation between the ordered rock salt structure of the former and the ribbon structure of the latter is explained on the following basis: both structures can be described as strips built up as an assembly of infinite ribbons of MoO_6 octahedra that are five octahedra thick, and that differ by slight displacements of the octahedral ribbons. We show that the electrochemical behavior of the $Li_xMo_5O_{17}$ system is based on two sorts of Li^+ sites; those that are located within the strips between the ribbons, and those that are located at the border of the strips. The high rate of Li intercalation in this oxide and its reversibility are discussed in terms of its peculiar structure.

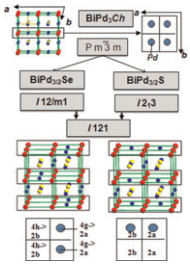

Structure relations for perovskite type $BiPd_3C$, $BiPd_{3/2}Se$ and $BiPd_{3/2}S$.

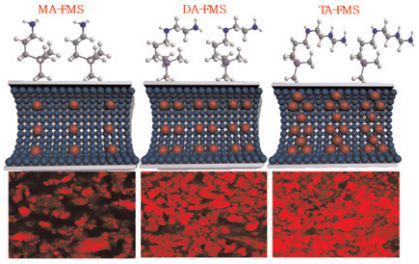

Control of electrostatic interaction for DNA biding by amino-functionalized modification: mono-amine (MA), di-amine (DA), and tri-amine (TA). The red-ball means the amine groups of FMS.

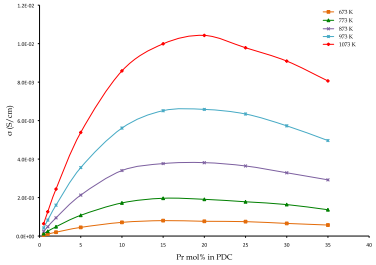

Ionic conductivity in praseodymium doped ceria as a function of dopant concentration calculated using the kinetic lattice Monte Carlo vacancy-repelling model, which predicts the optimal composition for achieving maximum conductivity.

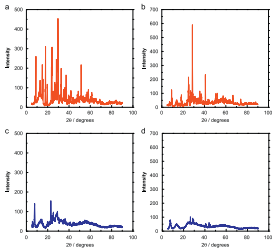

Powder XRD patterns of (a) PW_{18}, (b) $K[BMIM]_6H_4PW_{18}O_{62}$, (c) P_2W_{18}, and (d) $K_2[BMIM]_4P_2W_{18}O_{62}$.

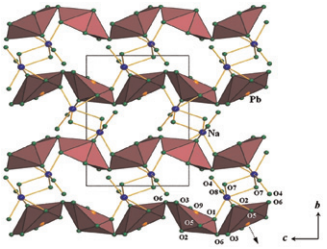

A new phase, $NaPbB_5O_9$, has been discovered in the ternary M_2O–PbO–B_2O_3 (M = alkali-metal) system. The crystal structure consists of a novel infinite $_\infty[PbO_6]$ chains.

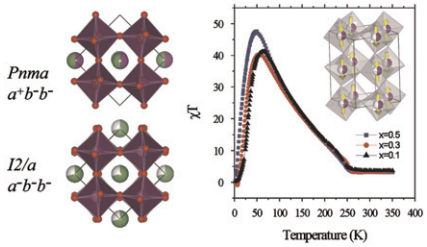

The influence of Bi^{3+} on the structural and magnetic properties of the rare-earth-containing perovskites $REFe_{0.5}Mn_{0.5}O_3$ (RE = La,Nd) was studied. Crystal structures in both La and Nd series were determined using X-ray and neutron diffraction to be $GdFeO_3$-type *Pnma* with the exception of the $Bi_{0.3}La_{0.7}Fe_{0.5}Mn_{0.5}O_3$ sample, which is monoclinic *I2/a* in the $a^-b^-b^-$ tilt scheme. The samples undergo a transition to G-type antiferromagnetic order along with a weak ferromagnetic component, mixed with the cluster-glass type behavior.

Continued

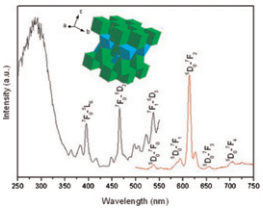

The excitation and emission spectra of Y_2WO_6:Eu^{3+} indicates the effect of long wavelength-excited property, which is ascribed to the cube coordination environment of Eu^{3+} ions with the uniform Eu–O bond length.

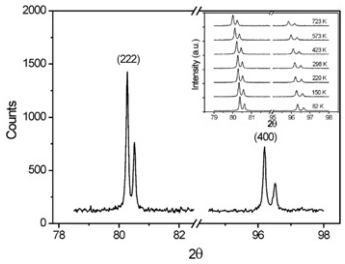

Enlarged sections of the X-ray diffraction pattern of Ba_2InTaO_6 showing the basic (222) and (400) reflections. Insert shows the evolution of these reflections as function of temperature. No peak splitting is observed in the temperature range between 82 and 723 K.

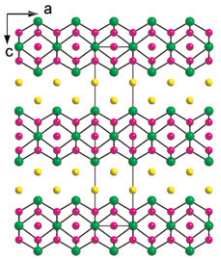

Two new K–Mg–Tt phases, $K_2Mg_{5-x}Sn_3$ ($x = 0.28$) and $K_3Mg_{18}Tt_{11}$ (Tt = Sn, Pb), have been synthesized and structurally characterized. $K_2Mg_{5-x}Sn_3$ is isostructural with $Ni_{7-x}SbQ_2$ (Q = Se, Te) and features a 2D corrugated $[Mg_5Sn_3]$ layer that is separated by K^+ cations, and $K_3Mg_{18}Tt_{11}$ (Tt = Sn, Pb) is closely related to the $Ho_2Rh_{12}As_7$ structure type and features a 3D $[Mg_{18}Tt_{11}]$ network with 1D hexagonal tunnels along the c-axis occupied by K^+ cations.

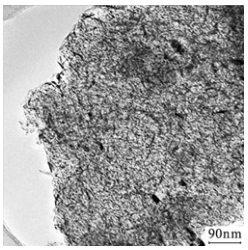

The mesoporous BN with a high specific surface area of 219 $m^2\ g^{-1}$ exhibits a strong luminescence emission around 3.41 eV in the CL spectra, high thermal stability in both morphology and structure, and good oxidation resistance up to 800 °C.

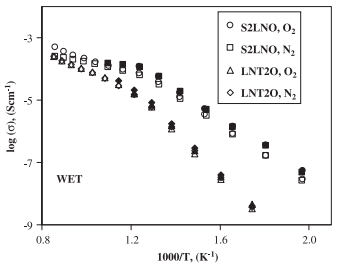

Comparison of total (open symbols) and bulk (closed symbols) conductivities measured in wet ($p(H_2O) \approx 0.026$ atm.) nitrogen and oxygen atmospheres for $LaNb_{0.98}Ti_{0.02}O_{4-\delta}$ (LNT2O) and $Sr_{0.02}La_{0.98}NbO_{4-\delta}$ (S2LNO) materials.

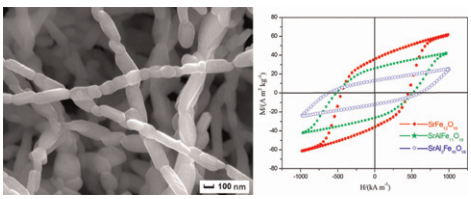

Al^{3+} ions substituted strontium ferrite nanofibers have been prepared by the electrospinning with a diameter of about 100 nm and the Al^{3+} ion substitution has a great effect on the microstructure and magnetic property of $SrAl_xFe_{12-x}O_{19}$ nanofibers.

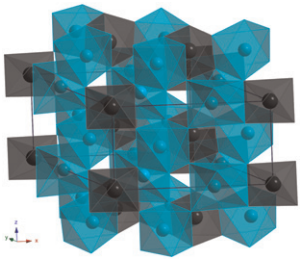

A complete solid solution between Tl_2TeO_6 and In_2TeO_6 is formed. A compositionally controlled metal–insulator transition occurs in $Tl_{2-x}In_xTeO_6$ at an x value of about 1.5. No superconductivity could be detected down to 5 K.

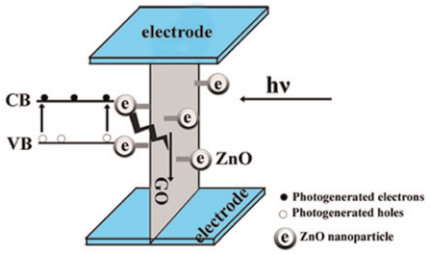

Upon irradiating the GO–ZnO sample with a light having an energy equalizing the band gap energy, the photogenerated charge–hole pairs are produced, and have been separated effectively.

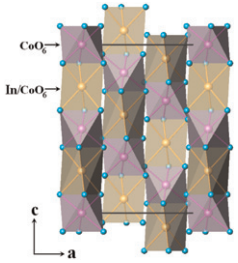

$Sr_3In_{0.9}Co_{1.1}O_6$ possesses 1D chains constructed by alternating face-sharing CoO_6 octahedra and $(In_{0.9}Co_{0.1})O_6$ trigonal prisms. The high spin Co^{3+} ($S=2$) in trigonal prism shows a g factor of 2.0.

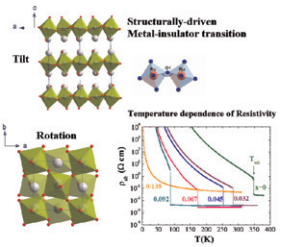

The metal–insulator transition temperature (T_{MI}) was drastically reduced by Cr doping, and is closely related to the distortion of structure.

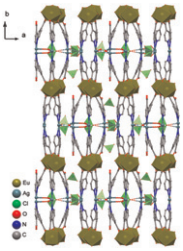

Two new anion-templated 2D 4*d*–4*f* Ln–Ag heterometallic coordination polymers based on novel lanthanide–carboxylate chains and pillared $Ag(IN)_2$ units, $\{[Ln_3Ag_5(IN)_{10}(H_2O)_7]\cdot 4(ClO_4)\cdot 4(H_2O)\}_n$ (*Ln* = Eu (**1**) and Sm (**2**), HIN = isonicotinic acid), have been hydrothermally synthesized and structurally characterized. **1** and **2** exhibit good luminescent properties.

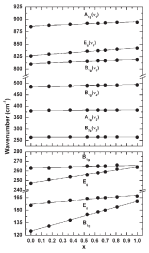

Plot of the observed wavenumbers of Nd:$Y_xGd_{1-x}(VO_4)$ versus Y content (x). The linear trend indicates that most of the observed wavenumbers exhibit a one-phonon-like behavior.

Continued

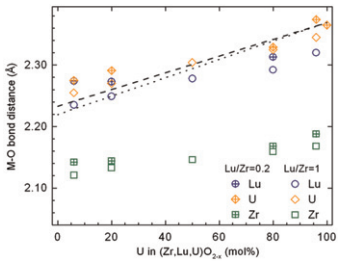

Metal–oxygen bond distances in $(Zr,Lu,U)O_{2-x}$ solid solutions with different oxygen vacancy concentrations (Lu/Zr = 1 and Lu/Zr = 0.5).

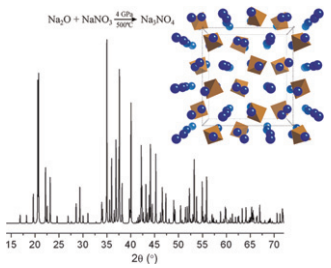

We studied Na_3NO_4 at high pressure using Raman spectroscopy and X-ray diffraction and determined $V(P)$ to 64 GPa. We investigated synthesis and phase behavior of the orthonitrate at high-P,T conditions.

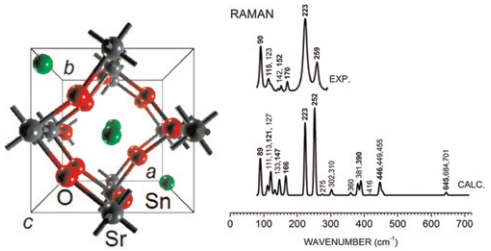

Orthorhombic $SrSnO_3$: a view of the unit cell (left) and plots showing the calculated and experimental Raman spectra (right).

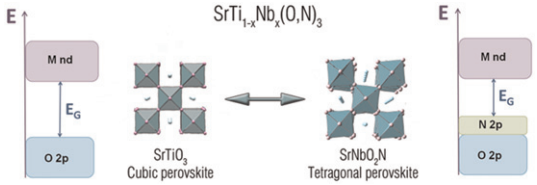

The system $SrTi_{1-x}Nb_x(O,N)_3$ is described and the changes in crystal structure, nitrogen content and width of the band gap are discussed.

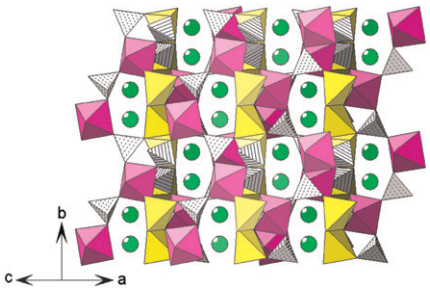

A projection along the [101] direction of the structure showing the six-edged tunnels, occupied by the K^+ ions.

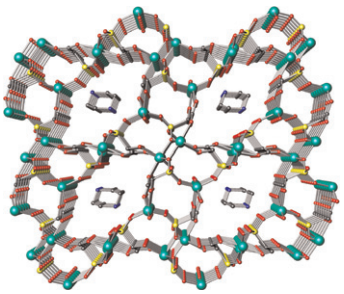

Six new metal phosphonates exhibit layered or 3D frameworks based on 2-hydroxyphosphonoacetate with five new coordination modes.

Rapid Communication

Preparation of magnetic $CoFe_2O_4$-functionalized graphene sheets via a facile hydrothermal method and their adsorption properties

Nianwu Li, Mingbo Zheng, Xiaofeng Chang, Guangbin Ji, Hongling Lu, Luping Xue, Lijia Pan and Jieming Cao

page 953

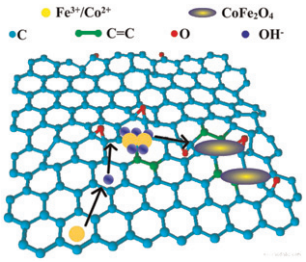

OH^- was recognized as a tie to integrate the inorganic salts with the graphene sheets, which made reaction started and developed on the surface of graphene sheets and formed cobalt ferrite nanoparticles on graphene sheets.